

Control of Coherent Structures via External Drive of the Breathing Mode¹

I. Romadanov^{a, b, *}, Y. Raitses^a, and A. Smolyakov^b

^a Princeton Plasma Physics Laboratory, Princeton, NJ 08543 USA

^b University of Saskatchewan, Saskatoon, SK S7N5E2 Canada

*e-mail: ivr509@mail.usask.ca

Received August 29, 2018; revised November 20, 2018; accepted November 22, 2018

Abstract—The Hall thruster exhibits two types of large-scale coherent structures: axially propagating breathing mode ($m = 0$) and azimuthal, with low m , typically $m = 1$, spoke mode. In our previous work, it was demonstrated that axial breathing mode can be controlled via the external modulations of the anode potential. Two regimes of the thruster response, linear and nonlinear, have been revealed depending on the modulation amplitude. In this work, using the high-speed camera images and developed image-processing technique, we have investigated the response of the azimuthal mode to the external modulations. We have found that, in linear regime, at low modulation voltages, axial and azimuthal structures coexist. At larger amplitudes, in the nonlinear regime, the azimuthal mode is suppressed, and only axial driven mode remains.

DOI: 10.1134/S1063780X19020156

1. INTRODUCTION

Hall thruster is an electric propulsion device, in which the thrust is generated by the axial acceleration of ions in a quasineutral plasma [1, 2]. This is achieved in the configuration with the magnetic field transverse to the applied electric field. The magnetic field is chosen sufficiently strong to keep electrons magnetized, thus preventing them from streaming to the anode, while ions remain only weakly affected by the magnetic field and can be accelerated by the electric field. Initial designs were prone to various instabilities, including azimuthal modes. A special profiling of the magnetic field suggested by A.I. Morozov [3] stabilized the most violent modes and allowed the development of the Hall thruster concept (so-called stationary plasma thruster (SPT)) into practical space flights applications in Russia under the general guidance of Morozov [4–6]. Two types of large-scale modes, axial breathing mode and azimuthal spoke, typically $m = 1$ (where m is the azimuthal mode number), are still fairly prominent in most of the thrusters. Their physics mechanisms are not fully understood, and their effects on thruster performance, in particular, the role of the breathing mode, is under discussion [7]. It is also believed that large-scale azimuthal structures conduct most of the anomalous current [8, 9]. Prominent role of the large-scale structures in thruster behavior and performance has long been the motivation for the development of the methods for control of the breath-

ing modes [10–14] and spokes [15]. Control of plasma behavior is an important topic, with a lot of practical applications [16–18]. Typical control methods are based on a feedback principle or on an active control by applying external forces or varying plasma parameters at certain frequencies [19]. Here, we briefly describe ways to control large-scale oscillations in Hall thrusters.

The breathing mode [20, 21] is normally associated with oscillations of the ionization front propagating in the axial direction with $m = 0$ and affecting the whole plasma volume. This mode can be crucial for the thruster operation and may lead to the termination of the discharge. In previous work, we have demonstrated the control of this mode [12, 13] by applying the external AC modulations (V_{mod}) to the DC anode potential U_d , which was set to 220 V in our experiments. It was found that thruster has two types of response on those modulations [7]. In the linear regime, when amplitude of the applied AC component is below 10% of the DC level, the root-mean-square (RMS) values of the ion and discharge currents and their oscillation amplitudes grow linearly with the increase of the modulation amplitude. One can see that the error bars for these points mostly overlap (Fig. 1a); therefore, changes in RMS values are negligible. In the nonlinear regime, the RMS of the discharge and ion currents and their oscillation amplitudes grow faster (nonlinearly) than the applied AC component. The amplitude of the discharge current

¹ The article is published in the original.

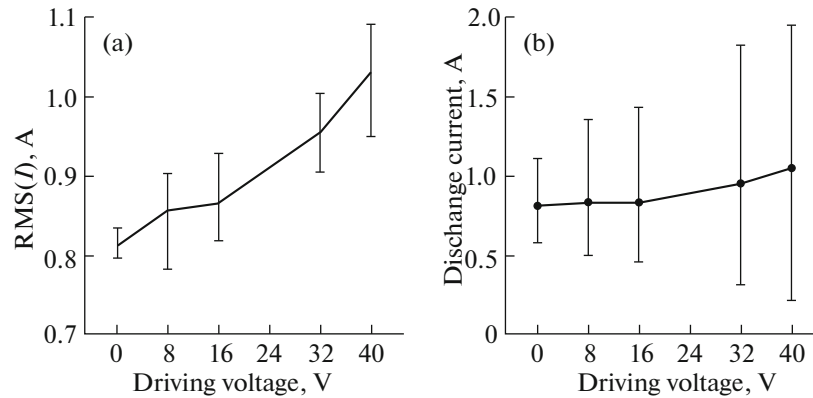


Fig. 1. (a) RMS values of the discharge current vs. driving voltage. The error bars represent the uncertainty of the discharge current measurements. (b) RMS values of the discharge current and corresponding amplitudes.

oscillations becomes much larger than in the linear regime (Fig. 1b).

It was demonstrated that, in the nonlinear regime, the breathing mode controlled by the external modulations leads to the increase of the current and propellant utilization [7]. It was shown that this effect has a resonant nature, as the RMS and the oscillation amplitudes reach the maximum at a certain frequency, which depends on the amplitude of the AC component.

Strong $\mathbf{E} \times \mathbf{B}$ flow of electrons and other plasma in homogeneities provide energy source for various other instabilities in Hall thrusters. In particular, they form large-scale azimuthal structures, namely, spokes [22] propagating in the azimuthal direction with $m = 1$ or higher [23, 24]. The spoke can cause the increase of the cross-field transport in a wide variety of devices with $\mathbf{E} \times \mathbf{B}$ fields, including Hall thrusters [25], Penning discharges [26], and magnetrons [27, 28]. For the Hall thruster, the current-conducting spoke is of special interest, because the anomalous transport affects the thruster efficiency [8].

While theoretical mechanism for the spoke formation is still not clear, there have been some attempts to control its appearance. The spoke can be suppressed by adjusting operational thruster parameters: the magnetic field profile [8, 9] and the cathode electron emission current [25]. Active control method was demonstrated in works by Nevrovskii by inducing oscillations on inserted in plasma electrode [29], as well as by Griswold et al. [9, 15] and Yuan Shi et al. [30] based on the feedback control of the voltage by use the segmented anode. It was implemented in the cylindrical Hall thruster (CHT). Experiments in [8] demonstrated that spoke suppression leads to the reduction of the total discharge current.

In this paper, we study the effect of external AC modulations on the azimuthal and axial modes. External modulations were applied at different amplitudes and frequencies, so thruster was operated in both lin-

ear and nonlinear regimes. It was earlier established that large-scale density and potential fluctuations are well correlated with plasma emission [8]. Therefore, the large-scale plasma structure, such as spoke and breathing modes, can be detected by the emission observation. In our experiments, the changes in plasma emission intensity inside the thruster channel were observed by the fast imaging camera. Both types of modes, the breathing and rotating spoke, contribute to changes of the emission intensity. Since the camera is located in front of the thruster, the collected signal is the light intensity integrated along the axial direction. Therefore, it is impossible to determine the axial spoke location; however, the difference between the $m = 0$ (from breathing modes) and $m = 1$ (from the spoke) structures can be identified from image analysis.

2. EXPERIMENT AND DATA ACQUISITION SYSTEM

Research was performed at Small Hall Thruster Facility (SHTF) at the Princeton Plasma Physics Laboratory (PPPL) [31, 32]. The vacuum vessel is about 1-m³ volume and equipped with a turbopump, so the background pressure did not exceed 70 μ Torr during the operation. Experiments were done with the CHT with a 2.6-cm-diameter 2.3-cm-long channel. [33, 34] CHT is the device with crossed electric and magnetic fields that create and accelerate a plasma jet. Thruster was operated at $U_d = 220$ V DC level of the applied potential between the anode and the cathode, with typical levels of the discharge current of $I_d \sim 0.6$ – 0.8 A. Xenon gas was used as a propellant, with the flow rates of 3.5 and 2 sccm through the anode and the cathode-neutralizer, respectively. Magnetic field was created by means of two electromagnetic coils, which operated in so-called “direct” magnetic configuration with a diverging magnetic field [35]. Details of the design and operation have been described elsewhere [36].

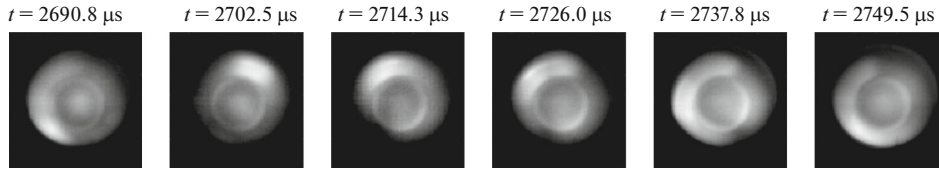


Fig. 2. A sequence of frames showing the light emission from the plasma in the CHT. Spoke is a region of increased light intensity propagating in the $\mathbf{E} \times \mathbf{B}$ direction (counter clockwise) in part masked by the presence of the $m = 0$ breathing mode with oscillations of the brightness across the whole channel.

Under the above conditions and configuration, CHT exhibits intrinsic breathing oscillations at ~ 13 kHz, the amplitude of the discharge current oscillations being about 0.1 A. Control of these oscillations was realized with the electric circuitry described in [7]. In brief, the sinusoidal AC component was added to the DC anode potential. Circuitry allowed to control the amplitude and frequency of modulation. The peak-to-peak amplitude of modulation V_{mod} was varied from 1 to 30 V. The frequency of modulation f_{mod} was varied between 10 and 15 kHz.

Light emission from the plasma during the thruster operation was captured with a Phantom Camera V7.3 in the visible spectrum. The camera frame rate was set at 87000 frames/s with 128×128 pixel resolution. Camera was located outside the vacuum chamber, looking in through a viewport that was ~ 1 m away from the channel exit and along the central plane of the thruster. Due to the location of the viewport, the camera was shifted off the thruster center line by approximately 15° . A rotating spoke is observed as a region with increased light intensity, which propagates in azimuthal direction corresponding to the $\mathbf{E} \times \mathbf{B}$ direction. A sequence of frames from the camera is shown in Fig. 2.

It is important to notice that discharge parameters were different from the ones used in previous studies of CHT [8, 9, 12, 15], which resulted in the reduction of spoke frequency from the 15–30 kHz range to the 5–8 kHz range in our experiments.

3. IMAGE PROCESSING

Axial mode can be identified relatively easily from the Fourier analysis of the global intensity over time; however, azimuthal mode is harder to detect. In previous studies, the special image processing technique in combination with Fourier analysis [37, 38] or the cross-spectral-density (CSD) techniques [39] were used for the detection of azimuthal coherent structures. Signal from plasma is contaminated by noise due to light emission from the walls and other parts of the thruster channel. The overlapping of axial and azimuthal modes, which exist simultaneously, results in spurious harmonics. As a result, identification of the coherent structures exclusively by the Fourier analysis or CSD is a difficult task. Additional complications

come due to semi-coherent nature of the azimuthal mode, which has some finite frequency spread (or frequency changes in time), in contrast to the breathing modes, which exhibit high coherency at a well-defined single frequency.

In our work, we implemented a combination of Fourier analysis and CSD techniques for azimuthal mode detection. Fourier analysis allows one to identify the range of frequencies of interest, which are used in CSD analysis. The CSD technique allows one to map spatial variations of the intensity onto the frame at different frequencies f_i . Output of this technique is information about phase shifts in the emission oscillations between different regions of the image, as well as information about coherence of these oscillations.

In our approach, spectrum of azimuthal and axial modes is defined initially from Fourier analysis. For $m = 0$ axial mode, the spectrum is obtained by taking a Fourier transform from global light intensity time series. The global light intensity is defined as a summation of all light intensities in one frame, effectively resulting in averaging over azimuthal direction. Finding spectrum of $m = 1$ mode requires some preprocessing of initial frames. Frames were cleaned from background light intensity, the oscillations due to axial $m = 0$ mode, and other noise. This part is similar to the technique which was used by McDonald [37, 38] and is described in the Appendix. Outcome of this stage is frames where $m = 0$ mode was subtracted and, then, the frequency and finite m azimuthal mode spectrum is obtained. Spectrum for azimuthal mode gives the range of frequencies of interest, where azimuthal structures can exist. The accurate identification of main frequency of the azimuthal modes is not always possible, due to some noise, and possibly due to some finite frequency spread in the azimuthal modes (non-stationary). The CSD technique is applied to further delineate the coherent structure of the azimuthal modes by calculating the CSD at each frequency of the interest.

The CSD at each frequency f_i is calculated as follows. The reference signal x_i and signals from each pixel y_i were divided into n_d nonoverlapping blocks with length T_d . For each block, the Fourier transforms X_i and Y_i for reference pixel and pixel of interest are

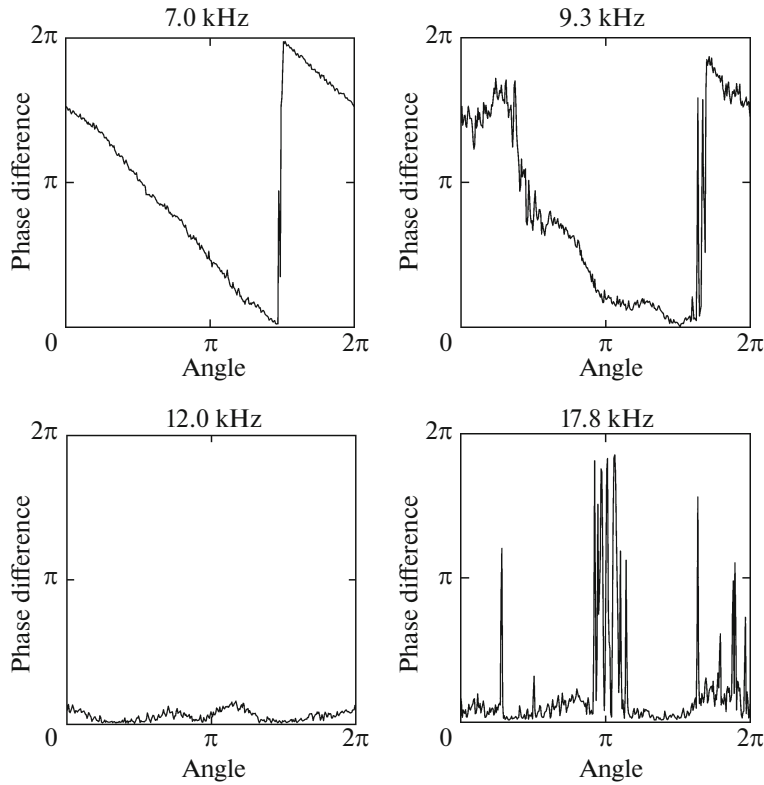


Fig. 3. Phase difference with respect to reference pixel as a function of azimuthal position (angle). Panel for 7.0 kHz shows the dependence for a spoke mode, panel for 12.0 kHz shows the dependence for a breathing mode, and panels for 9.3 and 17.8 kHz are chosen to show the difference between the frequencies related to coherent structure and arbitrary frequencies.

calculated respectively. The following definition for CSD is used:

$$\hat{G}_{xy}(f_i) = \frac{2}{n_d T_d} \sum_{i=1}^{n_d} X_i^*(f_i) Y_i(f_i),$$

where $n_d = 10$ and $T_d = 512$ were taken. Phase difference between two signals can be defined from the phase angle of complex $\hat{G}_{xy}(f_i)$ value. The coherence is then defined as follows:

$$C_{xy} = \frac{|\hat{G}_{xy}|^2}{\hat{G}_{xx} \hat{G}_{yy}},$$

where \hat{G}_{xx} and \hat{G}_{yy} are auto-spectral densities of x_i and y_i signals. In our analysis, the mean cross-coherence parameter is defined as follows:

$$C_m = \frac{\sum_{x,y} C_{xy}}{M \times N},$$

where M and N are frame sizes in pixels.

Specifically, the CSD algorithm is implemented as follows. First, the random pixel is selected on the frame, and its intensity variation over time is extracted. Then, by calculation the cross-spectral-

density, as described above, differences in phases and coherence between the intensity signal of the reference pixel and other pixels signals were obtained. After all those steps, one has 2D maps of relative coherences and phase differences between the reference pixel and all other pixels for each frequency. In the next step, the coherence maps were averaged for each frequency; therefore, coherence as a function of frequency is obtained. Modes that have highest averaged coherence are selected. Phase maps are essentially an image where value of each pixel represents the phase difference between signal from this pixel and the reference signal. Each pixel position is the same as in real image. This technique was adopted from [38], where detailed description is given.

The CSD diagnostic is illustrated in Fig. 3 with the synthetic signal, which contained spoke mode at 7.0-kHz frequency, and 12.0-kHz breathing mode. Spoke mode was simulated as a circle with Gaussian distribution of the intensity. The spoke radius was chosen to 1/3 of the channel radius. Intensity of the breathing mode changes as a sine wave. Additional Gaussian noise was added on the top of this video. This signal was analyzed with developed algorithm, and results are presented in Figs. 3 and 4.

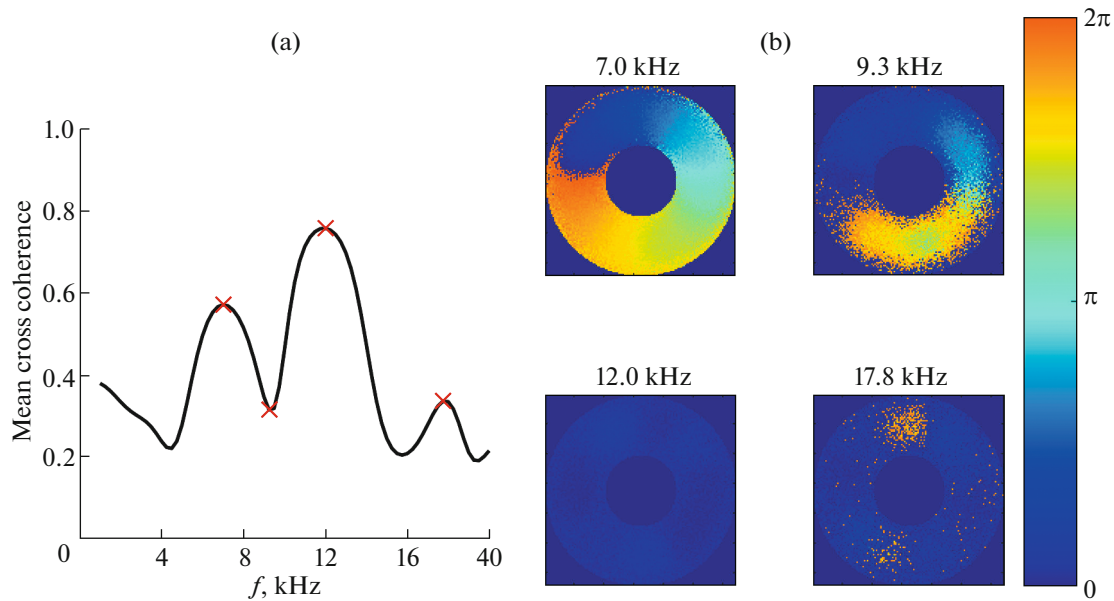


Fig. 4. (a) Mean cross coherence as a function of frequency. Frequencies for which the phase maps were plotted are marked with red crosses. (b) Phase maps for selected frequencies. Different colors represent different values of the phase shift, according to the color bar.

Figure 3 shows phase difference between the reference pixel and other pixels located at the same radius as a function of the azimuthal position (angle) for selected frequencies. For azimuthal mode, at 7.0-kHz frequency, phase difference should depend linearly on azimuthal position, changing from 0 to 2π with respect to the reference pixel. If plot it in cylindrical coordinates, this would look like a helix, which behavior is independent on radius. For axial mode, at 12.0 kHz, light intensity should change in phase independently on azimuthal position, meaning that the phase difference should be either 0 or 2π . This can be seen in Fig. 4 for 12.0-kHz mode. Frequencies 9.3 kHz and 17.8 kHz were chosen to illustrate the difference between the frequencies related to coherent structure and arbitrary frequencies. Phase difference dependence on azimuthal position for them has an intermediate behavior between spoke and breathing modes.

To illustrate how the mean cross coherence depends on selected frequency, it was calculated for the range of frequencies between 1.0 and 20.0 kHz. Figure 4a shows mean cross coherence C_m as a function of frequency and phase maps (Fig. 4b) for frequencies from Fig. 3. There are two prominent peaks (see Fig. 4a), related to the spoke and breathing modes, marked with red crosses. For the spoke mode on 2D map, we expect to see projection of helices with different radii. Color on such maps represents corresponding value of the phase shift in radians. Therefore, a smooth azimuthal transition from 0 to 2π with respect to the reference pixel will be obtained. This is shown in Fig. 4b for 7.0-kHz frequency. For breathing

mode, all pixels change their intensity in phase and their phase difference should be either 0 or 2π , as shown in Figs. 3 and 4b for 12.0-kHz frequency, where all phases are close to 0. It is important to notice that the method has an error; therefore, colors on phase maps are not completely uniform, as it should be for global modes. Other frequencies show the behavior which is a combination of spoke and breathing mode patterns, because this method is sensitive for higher harmonics of each signal, as well as their linear combinations.

Thus, peaks on coherence plots and shape of the phase map for these peaks are our main criteria to identify coherent structures in real signal.

4. IDENTIFICATION OF BREATHING AND SPOKE STRUCTURES IN CHT

First, we applied our analysis to the experimental data for the case without external modulations, so intrinsic breathing and spoke modes could be identified. Fourier spectrum for both modes is shown in Fig. 5. One can see that the global intensity (averaged over all finite m) oscillations show distinct frequency peak due to the presence of intrinsic axial oscillations at frequency around 13 kHz, as shown in Fig. 4a. On the contrary, finite m modes have several peaks distributed around 8 kHz (see Fig. 4b). We select several most prominent peaks (with amplitude >0.6 of maximum) and determine coherence for these peaks with CSD algorithm.

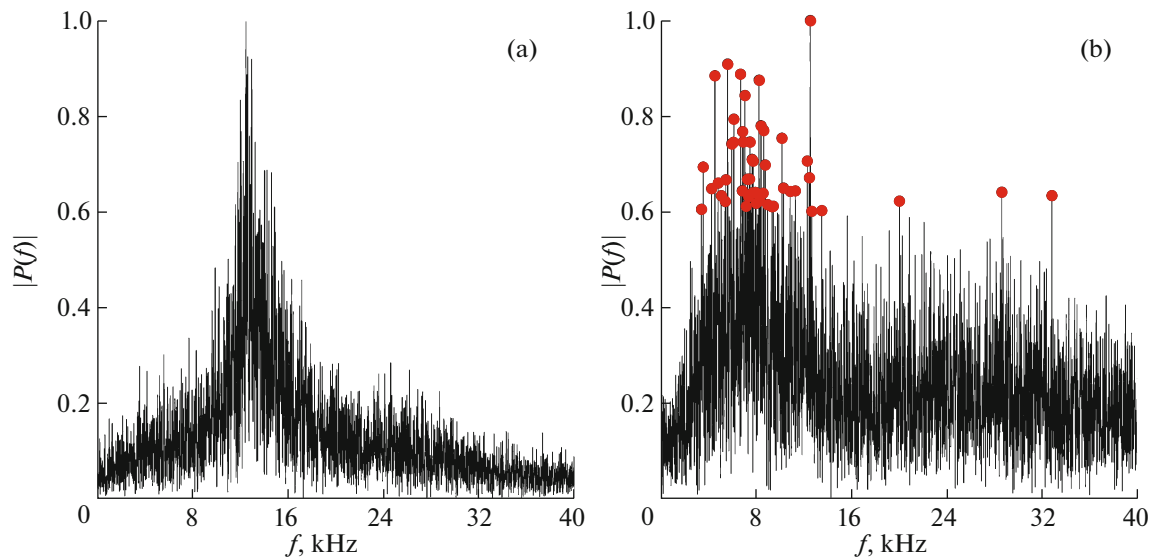


Fig. 5. (a) Spectrum for global intensity for $m = 0$ and (b) spectrum for azimuthal mode $m = 1$. Each plot is normalized to the highest amplitude. No modulation is applied. Red circles mark peaks with the most prominent frequencies (with amplitude >0.6 of maximum).

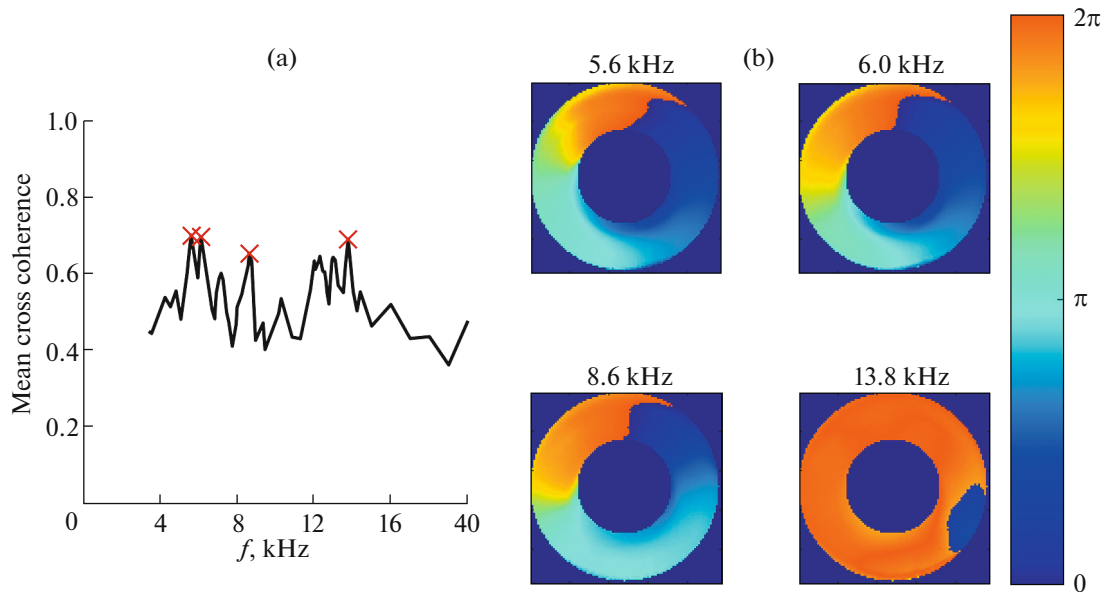


Fig. 6. (a) Averaged coherence value for the range of frequencies of interest from Fig. 4b. Red crosses show frequencies with large averaged coherence. (b) Phase maps for the most coherent frequencies (marked with red crosses on the left panel). The colors representing different phase shift values as shown on the color bar.

Results of the CSD mapping are shown in Fig. 6. Figure 6a represents an averaged coherence for each selected frequency from Fig. 5b. As one can see, not all frequencies from Fourier analysis have high coherence. Now, only frequencies with high coherence (greater than 0.65) were selected. They are marked with red crosses in Fig. 6a.

For these frequencies, the phase maps were plotted, as shown in Fig. 6b. There are three peaks which show high coherence at 5.6, 6.1, and 8.6 kHz. Phase maps for all of them indicate the existence of azimuthal coherent structures. Phase difference changes linearly in azimuthal direction from 0 to 2π with respect to the reference pixel. These modes move in azimuthal direction and corresponds to $m = 1$ mode

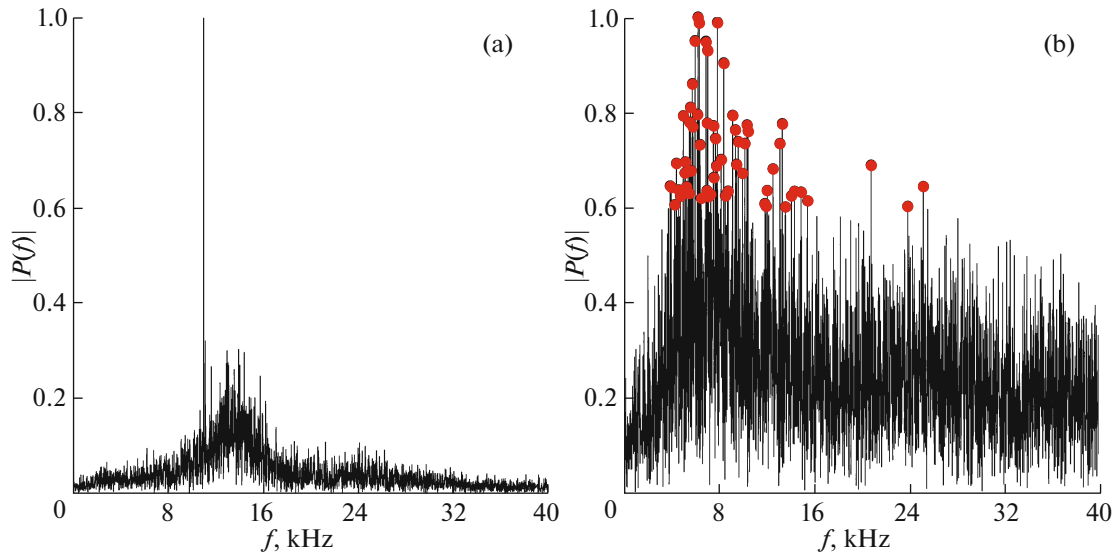


Fig. 7. (a) Spectrum for global intensity for $m = 0$ and (b) spectrum for azimuthal modes $m = 1$ at 5-V 10-kHz modulation. Each plot is normalized to the highest amplitude. Red circles mark peaks with the most prominent frequencies (with amplitude >0.6 of maximum).

(see Fig. 4b, 7.0 kHz for the reference). This mode is nonstationary, as its frequency changes over time; therefore, the range of frequencies is observed. At frequency about 13.8 kHz, there is a global $m = 0$ mode, which cause all pixels to change their intensity in phase (either 0 or 2π phase difference). Therefore, both $m = 0$ and $m = 1$ modes coexist at these operation parameters.

After the natural breathing and spoke modes were identified, the external modulation was applied. We started from linear regime with 5-V amplitude and frequencies at 10 and 15 kHz. Spectrum for $m = 0$ and higher m modes at 10-kHz modulations are shown in Figs. 7a and 7b, respectively. Spectrum for $m = 0$ shows that there is an intrinsic axial mode at about 13 kHz and a sharp peak at 10 kHz due to modulation (see Fig. 7a). Spectrum for azimuthal modes (see Fig. 7b) has again multiple peaks in the range of frequencies from 6.0 to 8.0 kHz, similar to the case without external modulations. The range of frequencies was selected with peaks higher than 0.6 of the maximum value, and the coherence was determined for each frequency.

Coherence for each selected frequency is shown in Fig. 8a. There are two strong peaks related to intrinsic axial mode (~ 13.9 kHz) and modulation frequency (10 kHz). For azimuthal modes, there are two peaks at 5.8 and 6.2 kHz. Phase maps at these frequencies confirm that this is the azimuthally propagating $m = 1$ mode, as there is a smooth transition from 0 to 2π (see Fig. 4b for the reference). Spoke mode is still nonstationary; however, range of frequencies is narrower in this case and this range overlaps with the natural $m = 1$ mode frequency range. The intrinsic breathing mode

is unchanged and exist at the same frequency of ~ 13.9 kHz.

Spectra at 5-V 15-kHz modulation are presented in Figs. 9a and 9b. Spectrum for the $m = 0$ mode is almost the same as in previous case, except for the modulation peak at 15.0 kHz. Spectrum for the azimuthal modes shows multiple peaks located in the same region of 6.0–8.0 kHz. Frequencies with peaks higher than 0.6 are selected for the CSD analysis.

Analysis of coherences and phase shifts is shown in Fig. 10. There is a strong peak related to external modulations at 15 kHz and several smaller peaks at frequencies of natural breathing. Phase maps show that pixel intensity changes at these frequencies in phase. Phase maps for two peaks at 5.8 and 7.5 kHz shows that phase changes smoothly from 0 to 2π for both frequencies (see Fig. 4b for the reference); therefore, there is a nonstationary spoke mode with $m = 1$, whose frequency changes in time.

In general, as illustrated in Figs. 8 and 10, external modulations at frequencies of the intrinsic breathing mode in linear regime has no effect on the axial or azimuthal modes. In all cases, the breathing, spoke, and external modulation frequencies are clearly present in the linear regime.

The next set of experiments was conducted in nonlinear regime with the amplitude of the external modulations of 30 V. First, the 15.0-kHz frequency, which is higher than the natural axial mode frequency, was used. Fourier spectra for $m = 0$ and finite m modes are shown in Fig. 11. There is a strong peak at 15.0 kHz for modulation signal and some small peaks related to the intrinsic breathing oscillations at ~ 13 kHz. For azimuthal m spectrum, there is a significant difference in

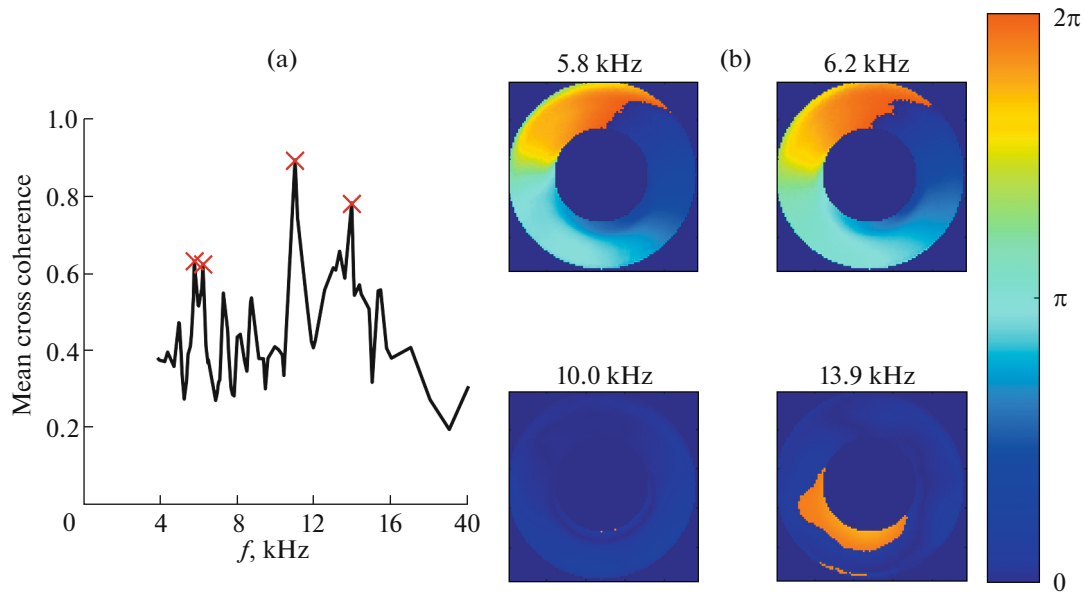


Fig. 8. (a) Averaged coherence value for the range of frequencies of interest from Fig. 6b. Red crosses show frequencies where averaged coherence reaches its maximum. (b) Phase maps for most coherent frequencies (marked with red crosses on the left panel). The colors representing different phase shift values as shown on the color bar.

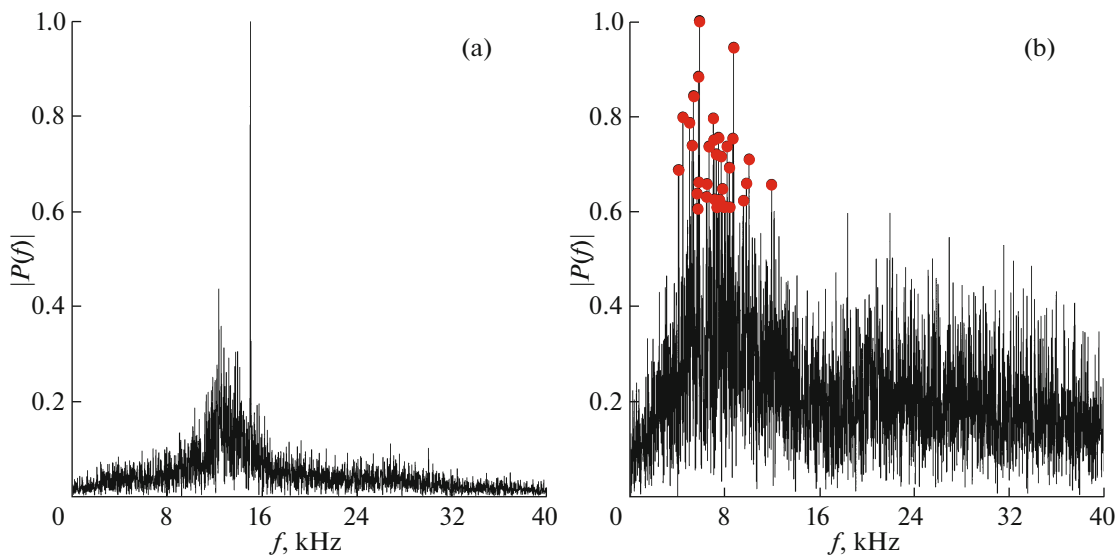


Fig. 9. (a) Spectrum for global intensity for $m = 0$ and (b) spectrum for azimuthal modes m at 5-V 15-kHz modulation. Each plot is normalized to the highest amplitude. Red circles mark peaks with the most prominent frequencies (with amplitude >0.6 of maximum).

the spectrum structure. There are peaks in a range of 6.0 to 8.0 kHz; however, spectrum is much noisier compared to linear regime or natural oscillations and it is difficult to identify any prominent frequencies. For CSD analysis all peaks with amplitudes higher than 0.6 were selected.

Results of the CSD analysis are shown in Fig. 12. There are peaks on coherence plot which correspond

to natural axial mode at ~ 12 – 13 kHz and modulation at 15.0 kHz. However, there are no prominent peaks in the region where azimuthal peaks existed. Phase maps show the existence of the intrinsic breathing mode at ~ 12 kHz, as well as the effect of oscillations at 15 kHz. Several frequencies were chosen between 5.0 to 8.0 kHz to show that there is no spoke mode in this case. It becomes clear if compare these phase plots

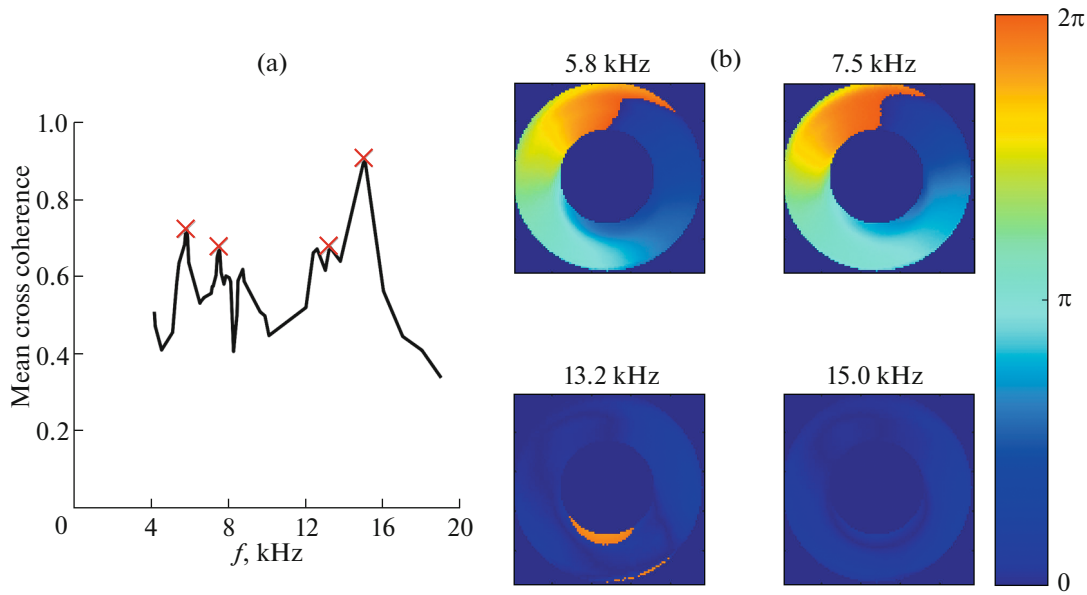


Fig. 10. (a) Averaged coherence value for the range of frequencies of interest from Fig. 8b. Red crosses show frequencies where averaged coherence reaches its maximum. (b) Phase maps for most coherent frequencies, marked with red crosses. The colors representing different phase shift values as shown on the color bar.

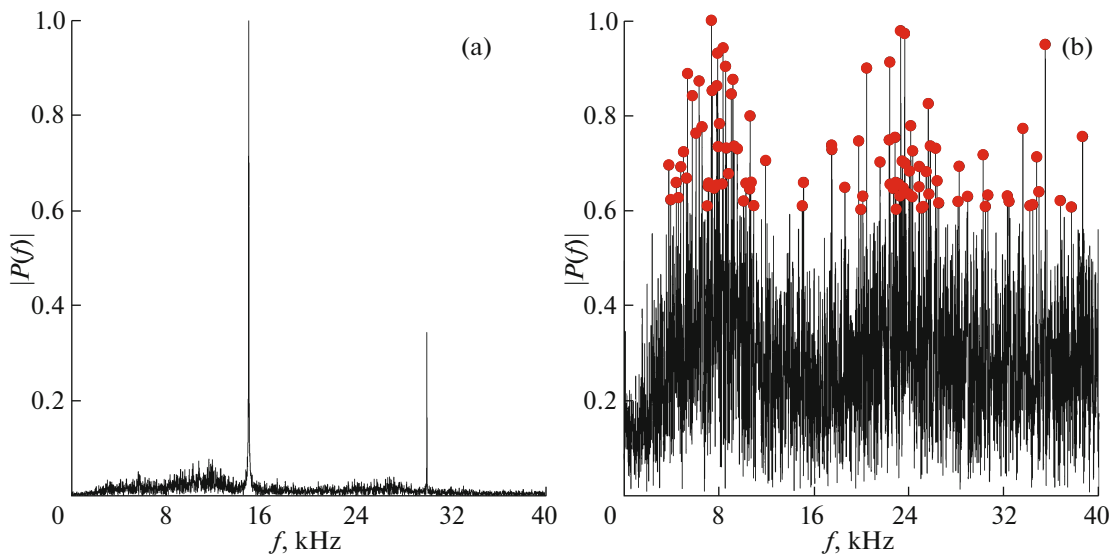


Fig. 11. (a) Spectrum for global intensity for $m = 0$ and (b) spectrum for azimuthal modes m at 30-V 15-kHz modulation. Each plot is normalized to the highest amplitude. Red circles mark peaks selected for the CSD analysis (with amplitude >0.6 of maximum).

with plot for 7.0 kHz in Fig. 4b. There is no smooth transition from 0 to 2π in azimuthal direction.

Finally, modulations with 30-V amplitude and 10.0-kHz frequency were applied to the thruster. There are strong peaks related to modulation at 10.0 kHz and nonlinear harmonics on $m = 0$ mode spectrum (see Fig. 13a). However, there are no other visible peaks related to intrinsic breathing oscillations.

Spectrum for azimuthal modes, shown in Fig. 13b, shows very noisy spectrum for finite m mode, without any identifiable range of frequencies. As in previous case, peaks with amplitudes higher than 0.6 were selected and the CSD technique was applied.

The coherence plot and phase maps for the case of 30-V 10.0-kHz modulations are shown in Fig. 14. There is a strong peak at modulation frequency on the

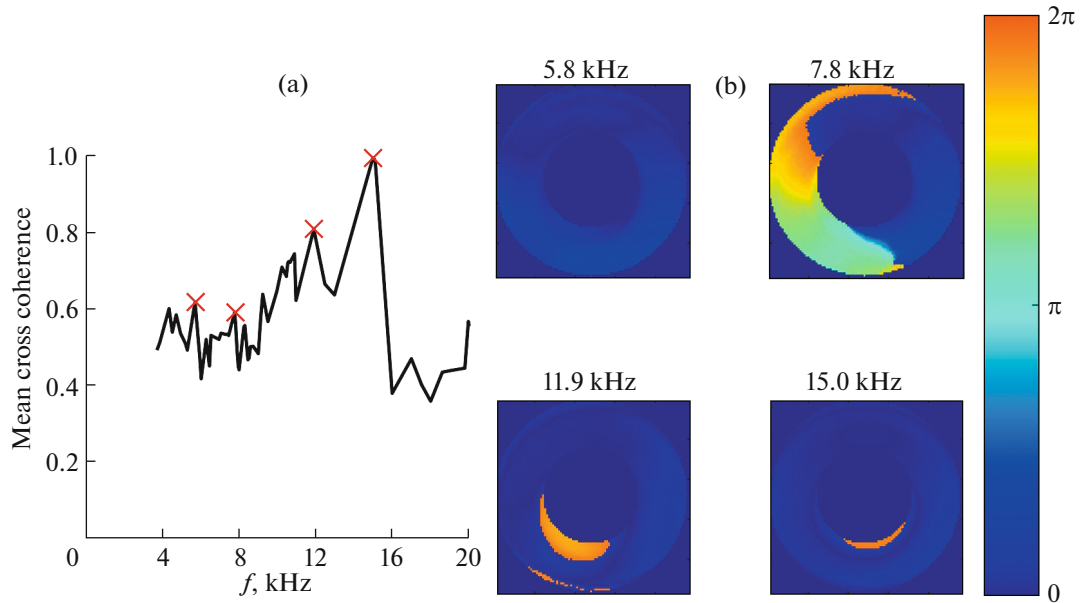


Fig. 12. (a) Averaged coherence value for the range of frequencies of interest from Fig. 10b. Red crosses shows frequencies related to the external modulation (15 kHz) and intrinsic breathing mode (12 kHz) and two frequencies in the range of natural spoke mode frequency (6–8 kHz). (b) Phase maps for selected frequencies, marked with red crosses. The colors representing different phase shift values as shown on the color bar.

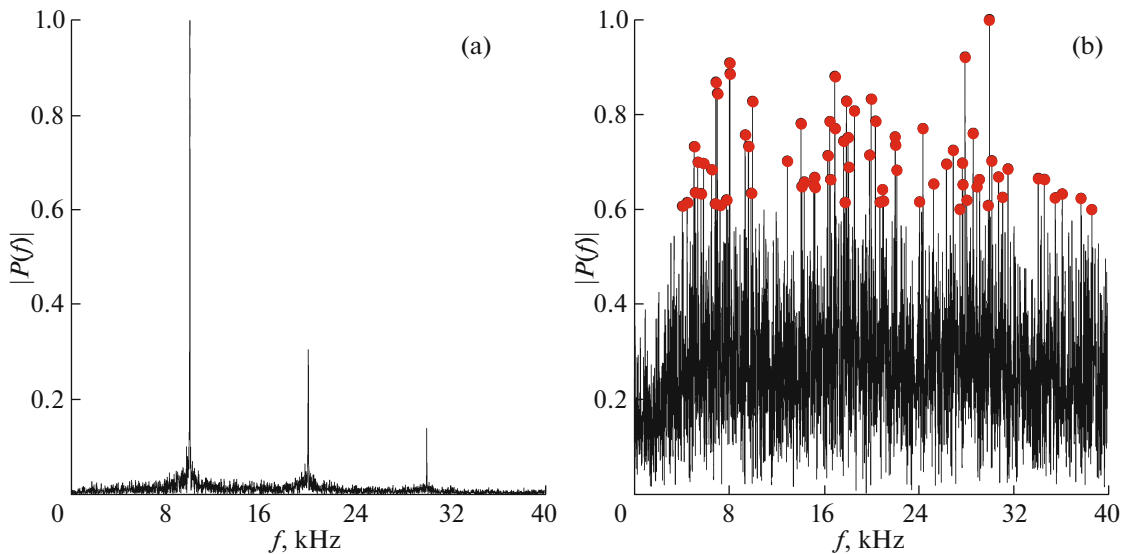


Fig. 13. (a) Spectrum for global intensity for $m = 0$ and (b) spectrum for azimuthal modes m at 30-V 10-kHz modulation. Each plot is normalized to the highest amplitude. Red circles mark peaks selected for the CSD analysis (with amplitude >0.6 of maximum).

coherence plot. No other coherent frequencies are identifiable from this plot. In order to plot phase maps, we chose several frequencies in the range of intrinsic spoke mode. Resulting phase maps are presented in Fig. 14b. As one can see, there are no azimuthal structures in this case (compare these phase maps to Fig. 4b).

5. CONCLUSIONS

In this work, we have demonstrated that the azimuthally rotating spoke mode can be suppressed by the external modulation of the anode potential at frequencies around natural breathing mode. Such behavior was captured by the combination of image processing techniques from [37–39], which allowed us to

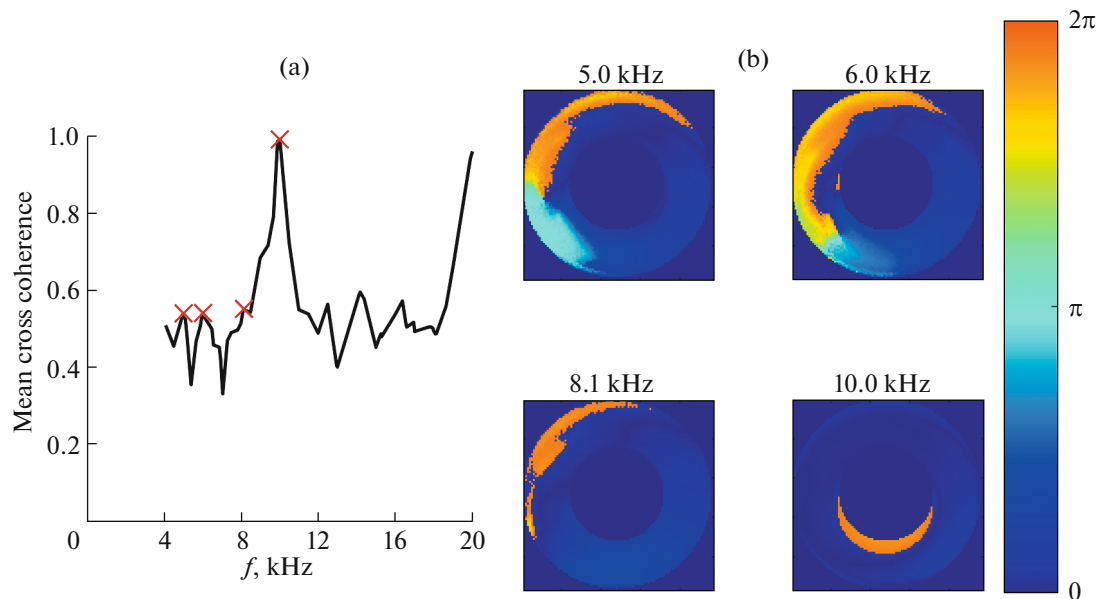


Fig. 14. (a) Averaged coherence value for the range of frequencies of interest from Fig. 12b. Red crosses shows frequencies related to the external modulation (10 kHz) and three frequencies in the range of natural spoke mode frequency (6–8 kHz). (b) Phase maps for selected frequencies, marked with red crosses. The colors representing different phase shift values as shown on the color bar.

identify coherent axial and azimuthal structures in the CHT during normal operation and with externally applied modulations of anode potential.

For normal operation, we identify coherent structures (breathing mode) in axial direction at ~ 13.9 kHz, whose frequency remains relatively stationary in time. Analysis of the azimuthally propagating structure (spoke mode) revealed that its frequency varied in the range of 5.8–8.5 kHz, which shows that the spoke mode is nonstationary, as its frequency changes over time.

External modulations were applied in the linear (5 V) and nonlinear (30 V) thruster response regimes. Modulation frequency was varied in each regime. In the linear regime, no effect on the intrinsic breathing and spoke modes was detected. Both modes have approximately the same frequencies as without modulations. In the nonlinear regime, azimuthal structures disappear at any modulation frequency in the range of 10–15 kHz.

Note that the driving of breathing oscillations in the nonlinear regime can suppress all low-frequency intrinsic modes, including breathing and spoke. In particular, it was also shown that, in the nonlinear regime (± 30 V) at a lower modulation frequency (10.0 kHz), the intrinsic breathing mode (13.9 kHz) disappears and no other coherent mode frequency (except the 10.0-kHz modulation) is observed.

These results show that there is an interaction between the azimuthal and axial modes. There exist several mechanisms that might be responsible for such

interaction. The azimuthal modes, such as spoke, are sensitive and can be driven by the axial gradients of plasma density and axial electric field (e.g., via the Simon–Hoh instability mechanism). Such axial gradients occur in the axial mode, such as breathing mode. The effectiveness of the coupling (interaction) will depend on the relative frequency spread between the modes. Additional coupling mechanism may also come from the interaction of ionization fronts [38]. Our experiments provide important evidence that the spoke may be suppressed by proper modulations of the axial parameters.

APPENDIX

DETAILS OF THE IMAGE PROCESSING TECHNIQUES

Recorded video can be considered as a 3D matrix of image pixel brightness as a function of position and time,

$$I = I(x, y, t),$$

where x and y are pixel column and row, respectively, and t is a time index. There are three main components of the video, which can be identified by looking at it. The first component is the image from the thruster channel itself and the background plasma, which gives some DC level of intensity. The second is oscillations of the intensity of the whole image due to the breathing mode, or $m = 0$ mode. The third is the azimuthal oscillations of the intensity due to the rotating spoke, or $m = 1$ mode, which are of the main inter-

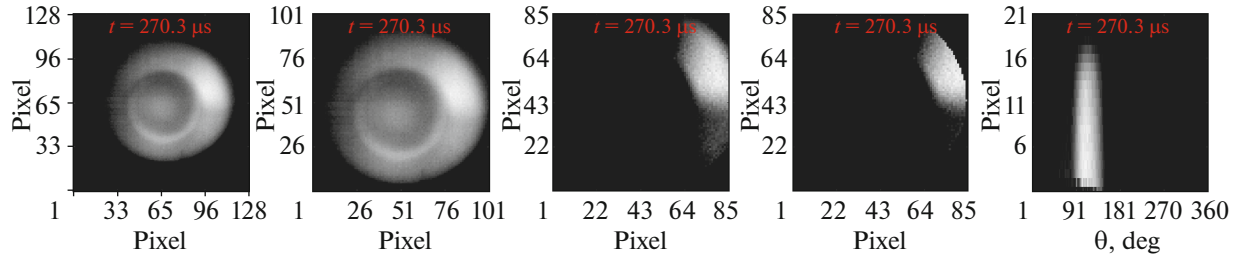


Fig. 15. Image processing stages at one time step. From the left to the right: raw image, cut by R_{ext} , removed background, applied mask and removed effect from the breathing mode, and image in polar coordinates.

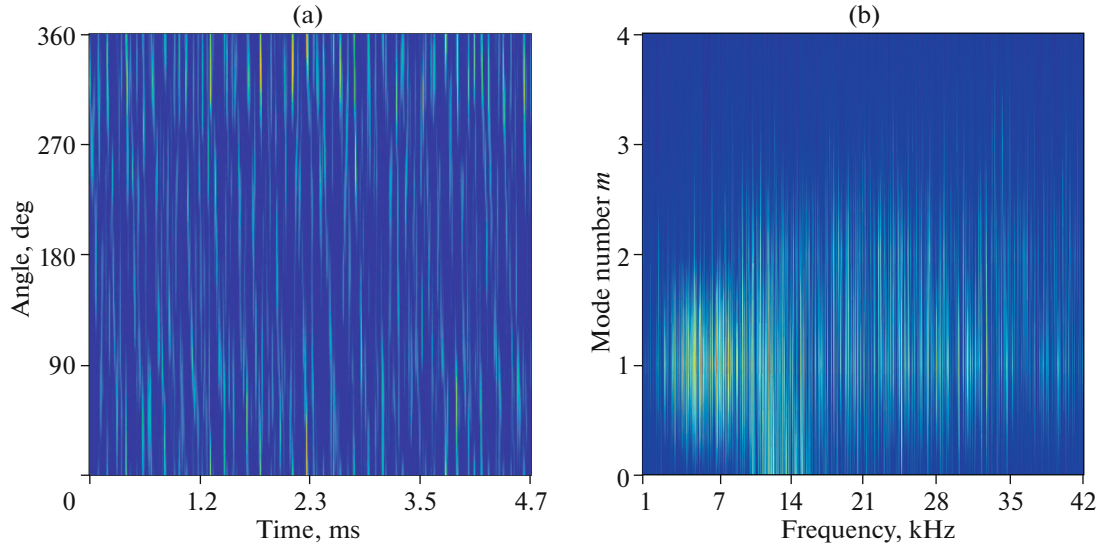


Fig. 16. (a) Spoke surface. The angled lines correspond to the spoke propagating in azimuthal direction with time. (b) 2D FFT matrix of the spoke surface. This matrix contains a discrete signal for each mode number. One can see that the $m = 0$ mode is still present even though it was cleaned out of the video. This happens because the breathing mode is much stronger than the azimuthal modes ($m = 1$).

est. To filter these oscillations from the DC level and $m = 0$ mode several steps were done. Stages of image processing are shown in Fig. 15.

The scheme of image processing includes the following steps.

1. Find external radius R_{ext} of the channel and the anode cup radius R_{int} . This is done by the MATLAB function “`imfindcircles`.”

2. Cut frames by the channel size.

3. Calculate mean DC level of all frames over time to obtain the mean image M , defined as

$$M(x, y) = \frac{1}{N_t} \sum_t I(x, y, t).$$

4. Subtract $M(x, y)$ matrix from each frame. Therefore, by subtracting it from each frame the background intensity is eliminated,

$$I_{\text{AC}}(x, y, t) = I(x, y, t) - M(x, y).$$

5. Apply circular mask on each frame by setting pixel values to zero within R_{int} and outside R_{ext} .

6. Split each frame on circles C_{it} with radius r_i and width of one pixel, so $R_{\text{int}} \leq r_i \leq R_{\text{ext}}$, and obtain $R_{\text{ext}} - R_{\text{int}}$ arrays of pixels.

7. Calculate average intensity of each circle as

$$c_i = \frac{1}{N_c} \sum_{\theta} C_{it}(\theta).$$

8. Eliminate breathing oscillation effect from each circle by subtracting average intensity c_i from each C_{it} array.

9. Transform each frame to polar coordinates,

$$I(x, y, t) \rightarrow I(R, \theta, t).$$

10. Because our analysis is focused on identifying the rotational structures, the radial dependence will be neglected. This is accomplished by average pixel

intensity along the radius. Therefore, the matrixes $I_{\text{avg}}(\theta, t)$ are obtained,

$$I_{\text{avg}}(\theta, t) = \frac{1}{R_{\text{ext}} - R_{\text{int}}} \sum_{r=R_{\text{int}}}^{R_{\text{ext}}} I(r, \theta, t).$$

11. Such matrices can be combined along time dimension in so-called 2D “spoke surface.” This surface represents variation of pixel intensity in angular direction θ and with time t .

12. In order to determine characteristic frequencies of azimuthal modes, the 2D Fourier transform was applied to it. The particular implementation is based on the built-in “fft” command in MATLAB. Results are shown in Fig. 16.

13. Breathing mode was identified through the Fourier transform of the signal, which was defined as follows:

$$B(t) = \sum_{x,y} I(x, y, t).$$

ACKNOWLEDGMENTS

This work was supported by DOE. We acknowledge Yuan Shi, Scott Keller, Ahmed Diallo, and Igor Kaganovich for fruitful discussions and Alex Merzhevskiy for his technical support.

REFERENCES

1. A. Morozov, *Plasma Phys. Rep.* **29**, 235 (2003).
2. A. Morozov, A. Kislov, and I. Zubkov, *JETP Lett.* **7**, 172 (1968).
3. A. Morozov, Y. Esipchuk, A. Kapulkin, V. Nevrovskii, and V. Smirnov, *Sov. Phys. Tech. Phys.* **17**, 428 (1972).
4. A. Morozov, in *Proceedings of the 2nd All-Union Conference on Plasma Accelerators, Minsk, 1974*, Ed. by A. I. Morozov (Nauka i Tekhnika, Minsk, 1974), Vol. 1, p. 224.
5. A. I. Morozov, *Physical Principles of Space Electric Propulsion Thrusters* (Atomizdat, Moscow, 1978) [in Russian].
6. A. Morozov, in *Proceedings of the 23rd International Electric Propulsion Conference, Seattle, WA, 1993*, Paper IEPC-93-101.
7. I. Romadanov, Y. Raitses, and A. Smolyakov, *Plasma Sources Sci. Technol.* **27**, 094006 (2018).
8. C. Ellison, Y. Raitses, and N. Fisch, *Phys. Plasmas* **19**, 013503 (2012).
9. C. Ellison, Y. Raitses, and N. Fisch, *IEEE Trans. Plasma Sci.* **99**, 1 (2011).
10. A. Morozov, V. Nevrovskii, and V. Smirnov, *Sov. Phys.-Tech. Phys.* **18**, 344 (1973).
11. S. Barral, J. Kaczmarczyk, J. Kurzyna, and M. Dudek, *Phys. Plasmas* **18**, 083504 (2011).
12. S. Keller, Y. Raitses, and A. Diallo, in *Proceedings of the 50th AIAA/ASME/SAE/ASEE Joint Propulsion Conference, Cleveland, OH, 2014*, Paper AIAA 2014-3509.
13. I. Romadanov, Y. Raitses, A. Diallo, K. Hara, I. Kaganovich, and A. Smolyakov, *Phys. Plasmas* **25**, 033501 (2018).
14. V. V. Arsenin, *High Temp.* **8**, 1202 (1970).
15. M. E. Griswold, C. L. Ellison, Y. Raitses, and N. J. Fisch, *Phys. Plasmas* **19**, 053506 (2012).
16. J. B. Taylor and C. N. Lashmore-Davies, *AIP Conf. Proc.* **1**, 23 (1970).
17. H. P. Furth and P. H. Rutherford, *AIP Conf. Proc.* **1**, 74 (1970).
18. V. Arsenin and A. Chuyanov, *Sov. Phys. Usp.* **20**, 736 (1977).
19. H. Lashinsky and E. Dewan, *AIP Conf. Proc.* **1**, 199 (1970).
20. J. Fife, M. Martínez-Sánchez, and J. Szaboín, in *Proceedings of the 33rd AIAA Joint Propulsion Conference, Seattle, WA, 1997*, p. 3052.
21. A. Morozov and V. Savelyev, in *Reviews of Plasma Physics*, Ed. by B. B. Kadomtsev and V. D. Shafranov (Consultant Bureau, New York, 2000), Vol. 21, p. 203.
22. O. Koshkarov, A. Smolyakov, A. Kapulkin, Y. Raitses, and I. Kaganovich, *Phys. Plasmas* **25**, 061209 (2018).
23. Y. Esipchuk, A. Morozov, G. Tilinin, and A. Trofimov, *Sov. Phys. Tech. Phys.* **18**, 928 (1974).
24. A. I. Morozov, in *Plasma Accelerators*, Ed. by L. A. Artsimovich, S. D. Grishin, G. L. Grozdovskii, L. V. Leskov, A. I. Morozov, A. M. Dorodnov, V. G. Padalka, and M. I. Pergament (Mashinostroenie, Moscow, 1973), p. 85 [in Russian].
25. J. B. Parker, Y. Raitses, and N. J. Fisch, *Appl. Phys. Lett.* **97**, 091501 (2010).
26. J. Carlsson, I. Kaganovich, A. Powis, Y. Raitses, I. Romadanov, and A. Smolyakov, *Phys. Plasmas* **25**, 061201 (2018).
27. S. N. Abolmasov, *Plasma Sources Sci. Technol.* **21**, 035006 (2012).
28. T. Ito, C. V. Young, and M. A. Cappelli, *Appl. Phys. Lett.* **106**, 254104 (2015).
29. V. Nevrovskii, PhD Thesis (Kurchatov Institute, Moscow, 1971).
30. Y. Shi, Y. Raitses, and A. Diallo, *Plasma Sources Sci. Technol.* **27**, 104006 (2018).
31. Y. Raitses and N. Fisch, *Phys. Plasmas* **8**, 2579 (2001).
32. A. Smirnov, Y. Raitses, and N. Fisch, *J. Appl. Phys.* **92**, 5673 (2002).
33. Y. Raitses, A. Smirnov, and N. Fisch, *Appl. Phys. Lett.* **90**, 221502 (2007).
34. A. Smirnov, Y. Raitses, and N. Fisch, *J. Appl. Phys.* **94**, 852 (2003).
35. A. Smirnov, Y. Raitses, and N. Fisch, *Phys. Plasmas* **14**, 057106 (2007).
36. A. Smirnov, Y. Raitses, and N. Fisch, *IEEE Trans. Plasma Sci.* **36**, 2034 (2008).
37. M. McDonald and A. Gallimore, *IEEE Trans. Plasma Sci.* **39**, 2952 (2011).
38. M. McDonald, PhD Thesis (University of Michigan, Ann Arbor, MI, 2012).
39. A. Light, S. Thakur, C. Brandt, Y. Sechrest, G. Tynan, and T. Munsat, *Phys. Plasmas* **20**, 082120 (2013).